

Single-atom imaging of ^{173}Yb in optical tweezers loaded by a five-beam magneto-optical trap

O. Abdel Karim,^{1, 2, *} A. Muzi Falconi,^{3, *} R. Panza,^{3, 1} W. Liu,^{1, †} and F. Scazza^{3, 1, ‡}

¹*Istituto Nazionale di Ottica del Consiglio Nazionale delle Ricerche (CNR-INO), 34149 Trieste, Italy*

²*Department of Physics, University of Naples Federico II, 80138 Naples, Italy*

³*Department of Physics, University of Trieste, 34127 Trieste, Italy*

(Dated: August 24, 2025)

We report on the trapping and imaging of individual ytterbium atoms in arrays of optical tweezers, loaded from a magneto-optical trap (MOT) formed by only five beams in an orthogonal configuration. In our five-beam MOT, operating on the narrow $^1\text{S}_0 \rightarrow ^3\text{P}_1$ intercombination transition, gravity balances the radiation pressure of a single upward-directed beam. This approach enables efficient trapping and cooling of the most common ytterbium isotopes (^{171}Yb , ^{173}Yb and ^{174}Yb) to $\lesssim 20 \mu\text{K}$ at densities $\sim 10^{11} \text{ atoms/cm}^3$ within less than one second. This configuration allows for significantly reducing the complexity of the optical setup, potentially benefiting any ytterbium-atom based quantum science platform leveraging single-atom microscopy, from quantum processors to novel optical clocks. We then demonstrate the first single-atom-resolved imaging of the fermionic, large-spin isotope ^{173}Yb ($I = 5/2$), employing a two-color imaging scheme that does not rely on magic-wavelength trapping. We achieve a high single-atom imaging fidelity of $99.96(1)\%$ and a large survival probability of $98.5(2)\%$, despite large differential light shifts affecting all nuclear spin sublevels of the excited $^3\text{P}_1$ state involved in the cooling transition. The demonstrated capabilities will play a key role in future quantum simulations and computing applications with ^{173}Yb arrays.

I. INTRODUCTION

Optically trapped alkaline-earth-like atoms (AEAs) have become a leading platform for quantum information processing, quantum simulation, and quantum metrology. Owing to their metastable clock states and the decoupled nuclear spins of fermionic isotopes, AEAs provide robust and versatile qubit encodings [1–9], as well as stable frequency references, underpinning state-of-the-art optical clocks [10–13] and matter-wave interferometers [14, 15]. These features also make ultracold AEAs an unparalleled resource for the simulation of novel quantum many-body systems [16–20]. In particular, the fermionic isotope ^{173}Yb — with its nuclear spin $I = 5/2$ and strong magnetic interactions between clock states — gives access to highly symmetric $\text{SU}(N)$ models of orbital magnetism [16–18, 21–26], largely unexplored to date.

To fully exploit the potential of AEAs for quantum science applications, it is crucial to develop scalable and reliable methods for efficient atom cooling and trapping, compatible with high-resolution detection at the single-particle level. In recent years, optical tweezer arrays have enabled significant advances in the microscopic control and detection of individual AEAs [27–36], facilitating striking demonstrations of high-fidelity quantum operations [5, 37–39] and novel tweezer clock architectures [40–45]. Two isotopes of ytterbium, bosonic ^{174}Yb and fermionic ^{171}Yb , have been previously trapped in optical

tweezer arrays and imaged with high single-atom detection fidelity [29, 31, 32] — a key capability for quantum processors and simulators [46–48]. On the other hand, fermionic ^{173}Yb atoms have yet to be individually trapped or imaged.

In experiments with AEAs, atoms are loaded into optical tweezers from a cold atomic sample in a narrow-line magneto-optical trap (MOT), which conventionally utilizes a six-beam configuration requiring optical access along all three axes. This setup often conflicts with the high numerical aperture (NA) required from at least one side of the atomic sample, where one or more microscope lenses are positioned to allow for addressing and imaging atoms with sub-micron optical resolution. In this work, we demonstrate the loading of ytterbium atoms into optical tweezers from a MOT operating with five beams in an open-top configuration, where the downward beam is omitted and entirely replaced by gravity to provide the necessary confinement along the vertical direction. This approach, demonstrated so far for dysprosium and erbium [49], eliminates the need for more intricate beam arrangements, simplifying the experimental setup while maintaining high loading efficiency [50]. It is particularly advantageous for compact, tweezer-based quantum science platforms with single-atom resolution, where a microscope objective is essential.

We show that such five-beam configuration allows to achieve the density and temperature necessary to efficiently load an optical tweezers array with any of the most common ytterbium isotopes — ^{174}Yb , ^{171}Yb , and ^{173}Yb . Further, we demonstrate the high-fidelity imaging of individually trapped fermionic ^{173}Yb atoms, exploiting a two-color scheme to simultaneously yield sufficient cooling and photon scattering rates [27, 31, 51, 52], even in the presence of large tweezer-induced differential light

* These authors contributed equally to this work.

† Present address: Institute of Laser Spectroscopy, Shanxi University, Taiyuan 030006, China.

‡ E-mail: francesco.scazza@units.it

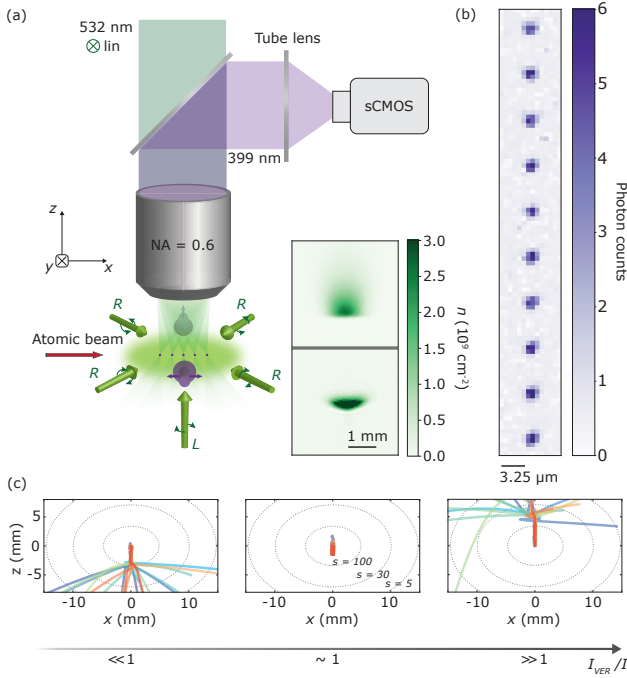


FIG. 1. Overview of the five-beam MOT and trapping of ytterbium atoms in optical tweezers. (a) Narrow-line MOT operating on the $^1S_0 \rightarrow ^3P_1$ transition at 556 nm in a five-beam configuration, where the top beam along gravity is omitted. The insets display absorption images of a ¹⁷⁴Yb MOT (top, 2 s loading) and cMOT (bottom, 0.7 s loading). Atoms are loaded into the optical tweezers array directly from the cMOT. A 0.6 NA objective is used to focus tweezer traps at 532 nm and to collect the atomic fluorescence on the $^1S_0 \rightarrow ^1P_1$ transition at 399 nm. A single horizontal retroreflected beam at 399 nm is employed to excite atoms, while the MOT beams are used to cool atoms during the imaging. (b) Average of 300 images of a tweezer-trapped ¹⁷⁴Yb atom array. (c) Monte Carlo simulations of single-atom trajectories in the five-beam MOT. Atoms are initialized at the intersection of the MOT beams and the dynamics is tracked for 200 ms. The MOT beam waists are 8 mm and 5 mm in the horizontal and vertical directions, respectively. Tuning the vertical beam intensity I_{VER} , we identify a regime where the average radiation pressure balances gravity holding the atoms without pushing them out of the MOT region. Dotted ellipses represent the intensity profile of one of the horizontal beams, described by the saturation parameter $s = I_{HOR}/I_s$.

shifts at our trapping wavelength of 532 nm. Despite the complex internal structure of ¹⁷³Yb and our peculiar five-beam molasses geometry, we achieve a high detection fidelity $> 99.95\%$ and low losses $\sim 1.5\%$, demonstrating single-atom imaging performances comparable to those obtained for ¹⁷¹Yb in similar trapping conditions using a conventional six-beam configuration [31]. Our technique could be extended to other high-spin alkaline earth atomic species, such as ⁸⁷Sr, possibly employing Sisyphus cooling instead of Doppler molasses to address a subset of the spin states.

An overview of our experimental setup is provided in Fig. 1(a). Within an octagonal glass cell, a five-beam

(5B) MOT operating on the narrow-line $^1S_0 \rightarrow ^3P_1$ transition at 556 nm ($\Gamma_{556}/2\pi = 182$ kHz) is loaded in 200 ms. Our MOT is loaded by an ytterbium atomic beam with average longitudinal velocity of about 40 m/s (see Appendix A for more details on the atomic source). We employ two crossed beams acting on the blue $^1S_0 \rightarrow ^1P_1$ transition at 399 nm ($\Gamma_{399}/2\pi = 29$ MHz) to further decelerate atoms below the narrow-line MOT capture velocity [53–55], avoiding the need of a broad-line MOT which is incompatible with a 5B configuration (see Section II). These beams cross horizontally around 22 mm upstream from the MOT center and are angled by 21° relative to the atomic beam direction. After loading, the MOT is compressed in 250 ms to increase its density and reduce its temperature before loading the optical tweezer array. The insets in Fig. 1(a) show the typical column densities of the 5B MOT and compressed MOT (cMOT) of ¹⁷⁴Yb, obtained via absorption imaging.

The one-dimensional tweezer array is generated using an acousto-optic deflector (AOD) working at 532 nm. We are able to generate up to 40 optical tweezers with an inhomogeneity below 2% at a minimum spacing around 1.3 μ m (see Appendix C). In typical experiments, we load tweezer arrays with a trap depth of about 2 mK and a spacing of 8.7 μ m from the 5B cMOT. The optical tweezer light is linearly polarized along the y -axis, and is focused onto the cold cMOT cloud by a custom microscope objective with $NA \simeq 0.6$ and an effective focal length of approximately 26 mm. Single-atom imaging is performed by illuminating the atoms with retroreflected, linearly polarized 399 nm light, with the forward and backward beams orthogonally polarized with respect to each other. The atomic fluorescence is collected using the same objective employed to focus the tweezer traps. The tweezer light and the atomic fluorescence are decoupled at the back of the objective using a dichroic mirror that transmits light at 532 nm and reflects light at 399 nm. The atomic fluorescence is then imaged onto a sCMOS camera (Teledyne Photometrics Kinetix22) using a 200 mm tube lens. The 5B MOT beams are turned on during imaging to provide molasses cooling of atoms trapped in the tweezer array (see Section III). Figure 1(b) shows a typical average image of a 10-tweezer array of ¹⁷⁴Yb, obtained from approximately 300 single-shot images.

II. FIVE-BEAM MOT

Compared to a conventional six-beam MOT, in a 5B configuration the down-propagating vertical beam is omitted and the upward push from the bottom beam is counteracted by gravity alone. This scheme leverages the interplay between narrow-line photon scattering and gravity, making it particularly effective for heavy atoms, such as lanthanides [49]. To gain insight into the 5B MOT working principle and verify its feasibility for ytterbium, we perform Monte Carlo simulations of the atomic trajectories in the MOT (see also Appendix B).

Trajectories are divided in time steps. For each step, we determine the photon scattering probability, taking into account the magnetic-field gradient, the detuning from resonance and the intensity profile of each MOT beam. Atomic coordinates are then updated considering the combined effects of gravity and stochastic single photon scattering events. Figure 1(c) displays 20 single-atom trajectories in three scenarios differing from one another by the vertical beam intensity. Atoms start at the intersection of the MOT beams, i.e. at the zero of the quadrupole magnetic field, and the trajectory is tracked for 200 ms. For $I_{\text{VER}} \ll I_s$, where $I_s \simeq 0.139 \text{ mW/cm}^2$ is the saturation intensity of the $^1\text{S}_0 \rightarrow ^3\text{P}_1$ transition, the vertical beam intensity is insufficient to hold atoms against gravity, causing them to fall downwards out of the MOT region. On the other hand, when $I_{\text{VER}} \gg I_s$ the atoms escape upwards due to the excessive radiation pressure from the bottom beam. At $I_{\text{VER}} \sim I_s$, the mean force from the upward beam balances gravity, allowing atoms to remain trapped in the MOT. This condition is achieved at an intensity around I_s as an outcome of the small linewidth of the $^1\text{S}_0 \rightarrow ^3\text{P}_1$ transition and the large mass of ytterbium. Indeed, lighter atoms would experience a stronger acceleration, thus requiring a weaker intensity, resulting in reduced robustness.

In a 5B MOT, unlike in a conventional six-beam (6B) MOT, the primary role of the vertical beam is to counteract gravity, while the horizontal beams must slow and capture the horizontally incoming atoms. Consequently, a 5B MOT greatly benefits from an unconstrained control on the horizontal and vertical beam intensities and detuning. Figure 2(a) illustrates the effect of the intensity I_{VER} and vertical beam detuning Δ_{VER} on the trapped number of atoms and the peak atomic density measured in a 5B MOT of ^{171}Yb after 2 s of loading. Consistently with the simulated atomic trajectories in Fig. 1(c), high intensities of the vertical beam lead to a lower number of captured atoms as they escape from the MOT vertically. Similarly, when the detuning is too close to resonance, the resulting scattering force becomes too strong, causing atoms to be pushed out of the MOT region. Notably, the atom number and peak density do not reach their maxima for the same conditions, since variations in the vertical beam parameters also affect the shape of the atomic cloud. In the top panel of Fig. 2(b), we present absorption images of the cloud for a fixed vertical beam intensity $I_{\text{VER}} \simeq 2 I_s$, corresponding to the dashed horizontal line in Fig. 2(a). For decreasing detuning from resonance, the cloud is pushed upwards in an unstable region above the center of the quadrupole field, leading to a reduced atom number. By increasing the detuning, on the other hand, the cloud shifts downwards as atoms redistribute to regions of the magnetic field gradient where the radiation pressure from the upward beam balances gravity. At the same time, the cloud develops into a drop-like shape, maximizing the total atom number while maintaining a nearly constant peak density. This behavior is confirmed in Monte Carlo simulations. In the bottom

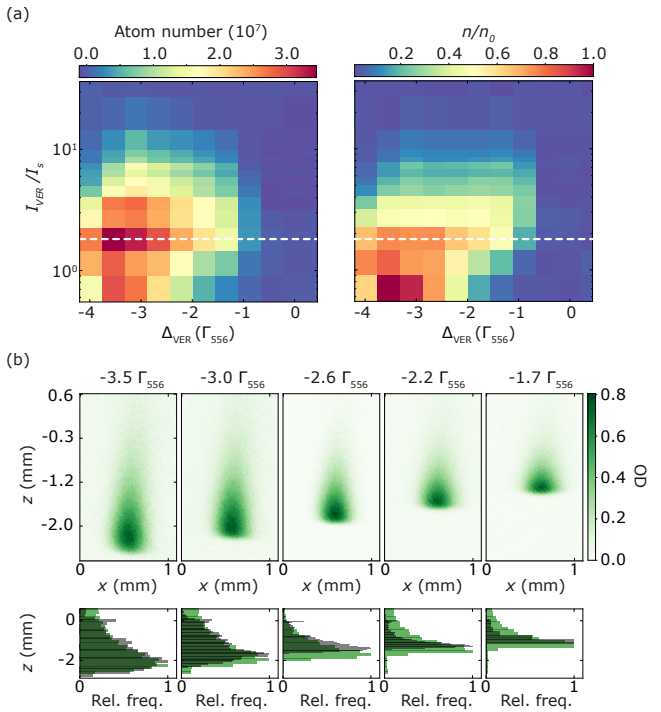


FIG. 2. Dependence of ^{171}Yb five-beam MOT loading on the vertical beam parameters. (a) Atom number captured by a ^{171}Yb 5B MOT (left) and normalized atom peak density n/n_0 (right) after 2 s loading time as a function of the vertical beam intensity I_{VER} and detuning Δ_{VER} . The magnetic field gradient is set to 5 G/cm, while the horizontal beams have a detuning of $\Delta \simeq -3.4 \Gamma_{556}$ and an intensity of $I_{\text{HOR}} \simeq 60 I_s$. (b) Top: in situ absorption images of the 5B MOT for different vertical beam detunings at fixed intensity $I_{\text{VER}} \simeq 2 I_s$, corresponding to the dashed line in panel (a). The cloud shifts downwards as the detuning moves away from resonance. Bottom: histograms of the experimental optical density (green) and of the simulated trajectories (grey) sampled on the z -axis. Each simulated histogram is the result of 20 independent trajectories. The zero of the z -axis in experimental images is set to optimally align them with simulations.

panel of Fig. 2(b) we compare the measured horizontally-integrated atomic densities with simulated distributions, obtained by binning the z -positions of 20 independent atomic trajectories for each detuning. We can approximate that each atom samples from all accessible states, since the atomic motion takes place on a timescale on the order of $h/E_{\text{rec}} \simeq 270 \mu\text{s}$ (E_{rec} is the atomic recoil energy from a 556 nm photon), much shorter than the total simulation time of 200 ms. We thus compare the entire simulated trajectory of a single atom with an experimental image of the MOT cloud observed at a specific time. The simulations reproduce both the vertical shift of the atomic cloud position and the asymmetric density profile broadening as a function of the vertical beam detuning.

Figure 3(a) reports the measured number of trapped atoms as a function of the overall beam detuning and magnetic-field gradient for ^{174}Yb and ^{171}Yb after 2 s of loading. The loading of fermionic ^{171}Yb ($I = 1/2$) dis-

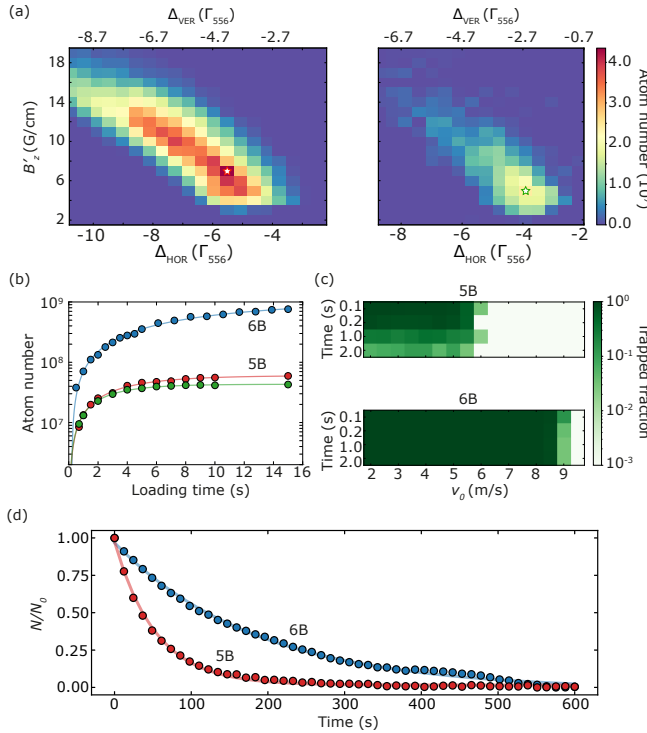


FIG. 3. Five-beam MOT loading and stability for bosonic and fermionic isotopes. (a) Atom number N as a function of horizontal and vertical beam detunings and magnetic-field gradient for ^{174}Yb and ^{171}Yb after 2 s of loading. The horizontal and vertical beam intensities are $220 I_s$ and $3 I_s$ for ^{174}Yb , and $60 I_s$ and $4 I_s$ for ^{171}Yb , respectively. For ^{174}Yb 6B MOT, the magnetic-field gradient and detuning Δ_{HOR} are set to 7 G/cm and $-4 \Gamma_{556}$, respectively. The values used for the 5B MOTs are marked by star symbols in panel (a). Solid lines represent exponential fits to the data (see text). (b) Loaded atoms as a function of time in a ^{174}Yb 6B MOT (blue circles) and a 5B MOT of ^{174}Yb (red circles) or ^{171}Yb (green circles). For ^{174}Yb 6B MOT, the magnetic-field gradient and detuning Δ_{HOR} are set to 7 G/cm and $-4 \Gamma_{556}$, respectively. The values used for the 5B MOTs are marked by star symbols in panel (a). Solid lines represent exponential fits to the data (see text). (c) Monte Carlo simulations of the capture and stability of a 5B and 6B MOT. We simulate the capture process for 100 independent atoms, entering the MOT region with variable velocity v_0 . The time-dependent captured fraction is determined as the number of atoms remaining in the MOT region after a variable holding time. The 5B and 6B simulations are performed using different beam intensities and detunings, optimizing the capture in each of the two cases. (d) MOT relative atom number N/N_0 as a function of holding time for ^{174}Yb , obtained in the 6B (blue circles) and 5B (red circles) configurations. Solid lines are exponential fits, yielding a lifetime $\tau_{6B} = 185(4)$ s and $\tau_{5B} = 54(1)$ s for the two configurations, respectively.

plays reduced robustness, which we attribute to the hyperfine and nuclear sub-structure of the $^1\text{S}_0 \rightarrow ^3\text{P}_1$ transition. In particular, the probability of scattering photons on the stretched $|F = 1/2, m_F = \pm 1/2\rangle \rightarrow |F' = 3/2, m'_F = \pm 3/2\rangle$ transitions is reduced with respect to the case of ^{174}Yb ($I = 0$). In Fig. 3(b), we compare the loading of a ^{174}Yb 6B MOT with that of ^{174}Yb and ^{171}Yb 5B MOTs. The loaded atom number N as a function of time is fitted with an exponential function,

6B (^{174}Yb)	5B (^{174}Yb)	5B (^{171}Yb)
τ_L (s)	12(1)	3.7(2)
$N_s (10^8)$	11.3(6)	0.61(1)
$R (10^8 \text{ s}^{-1})$	0.94(5)	0.164(3)
		0.176(1)

TABLE I. MOT loading rate parameters. Mean loading time τ_L , stationary atom number N_s and loading rate R , obtained from exponential fits of $N(t)$ for different isotopes and beam configurations.

$N(t) = N_s (1 - e^{-t/\tau_L})$, where N_s represents the stationary atom number and τ_L is the mean loading time. We can then define a loading rate, $R = N_s/\tau_L$, which quantifies the efficiency of atom collection. Table I reports the values of N_s , τ_L , and R for different isotopes and MOT configurations. We find that the 5B MOT atom number saturates faster and at a lower value N_s than for the 6B MOT, which indicates a reduced stability of the 5B configuration irrespective of the specific isotope. Additionally, the ^{171}Yb 5B MOT exhibits a shorter mean loading time and lower stationary atom number compared to ^{174}Yb , yet the loading rates are comparable. A MOT of ^{173}Yb also displays a similar change in the loading performance between the 6B and 5B configurations — with a reduction of N_s by nearly a factor of 10 yielding $N_s \sim 10^7$ for the 5B MOT. For all isotopes, we ascribe the reduced performance of the 5B MOT to an intrinsic residual loss mechanism, associated with the presence of an escape channel for atoms along the vertical direction. Specifically, fluctuations in the upward scattering force lead to atoms exiting the trapping region vertically and being lost [56]. Consequently, the 5B MOT reaches saturation in a shorter time τ_L with respect to the 6B configuration.

To investigate this behavior in more detail, we simulate the trajectories of 100 independent atoms entering the MOT region with different longitudinal velocities v_0 , and we determine the number of atoms remaining trapped in the MOT after a variable time from the start of the simulation. In simulations, we fix the beam parameters and magnetic-field gradient to optimal values, similar to the ones found in the experiment. Results for holding times comparable with the typical experimental loading times are shown in Fig. 3(c). For the same horizontal beam waist of 8 mm, the 5B MOT exhibits a lower capture velocity of about 5 m/s compared to 8.5 m/s of the 6B configuration. Moreover, unlike in the 6B MOT, the trapped fraction in the 5B MOT decays over time. In the 5B case, the reduced vertical beam intensity leads to preferential scattering from the horizontal beams (see Appendix B). When the horizontal intensity is too high, this imbalance causes atoms to fall out of the trap. To improve stability, the horizontal beam intensity must thus be reduced compared to the 6B case, resulting in a lower capture velocity. The reduced stability of the 5B MOT is thus confirmed in the individual trajectory approach of our simulations, which do not include the continuous loading of atoms during the holding time. The MOT sta-

bility can also be investigated by measuring its lifetime once the inflow of atoms from the atomic beam has been extinguished. In Fig. 3(d), we compare the lifetime measured for ^{174}Yb 5B and 6B MOTs. The fluorescence signal from the MOT is recorded over time using a CMOS camera, and the data is fitted with an exponential decay, yielding lifetimes $\tau_{6B} = 185(4)$ s and $\tau_{5B} = 54(1)$ s. While the reduction of the lifetime in the 5B configuration is significant, the lifetime remains sufficiently large — so as not to pose any issue for the following steps in the experimental sequence.

After loading, the 5B MOT is compressed in 250 ms to enhance the atomic density and reduce the temperature to values suitable for efficiently loading optical tweezer traps. During the compression, the center of the quadrupole field is gradually adapted using a vertical pair of bias coils to keep the 5B MOT fixed to its original position, despite the change of vertical beam intensity and detuning. We realize a 5B cMOT for ^{174}Yb , ^{171}Yb , and ^{173}Yb , reaching temperatures of $21(6)$ μK , $23(5)$ μK , and $9(2)$ μK , respectively, with typical mean densities around 10^{11} atoms cm^{-3} for all isotopes. The obtained temperatures for all isotopes are close to the Doppler temperature limit, $T_D = \hbar\Gamma_{556}/(2k_B) \simeq 4.4 \mu\text{K}$. The lower measured temperature for ^{173}Yb is likely the outcome of significant sub-Doppler cooling effects, associated to its high angular momentum structure [57].

III. LOADING AND IMAGING SINGLE ATOMS IN TWEEZER ARRAYS

We demonstrate the loading and high-fidelity imaging of single atoms in optical tweezers for bosonic and fermionic ytterbium isotopes. Here, we focus on ^{173}Yb , for which single-atom imaging has not been previously demonstrated. We load a 10-tweezer array at 532 nm from the 5B cMOT by turning on the traps during the whole MOT compression stage. Optical tweezers have a beam waist ($1/e^2$ -radius) of approximately 580 nm (see Appendix D) and a trap depth $\simeq 2$ mK. To achieve stochastic single-atom occupations, we induce light-assisted collisions (LACs) and consequent pairwise atom ejection [31, 58]. In particular, LACs are performed by applying a 50 ms red-detuned 556 nm pulse after loading the traps. To image single atoms, we employ a two-color scheme [27, 31, 51, 52]. We drive weakly the $^1\text{S}_0 \rightarrow ^1\text{P}_1$ transition for imaging, while simultaneously cooling on the $^1\text{S}_0 \rightarrow ^3\text{P}_1$ transition to preserve the atom inside the trap [29, 31, 51]. Imaging typically takes tens of milliseconds, determined by the interplay between the two mechanisms. As the linewidths of the two transitions are widely different ($\Gamma_{399}/\Gamma_{556} \sim 167$), the intensity of the imaging light must be sufficiently low to limit the photon scattering rate and the resulting heating. Figure 4(a) presents a single-shot image and an average over multiple realizations of a ^{173}Yb tweezer array. Images are obtained with an imaging

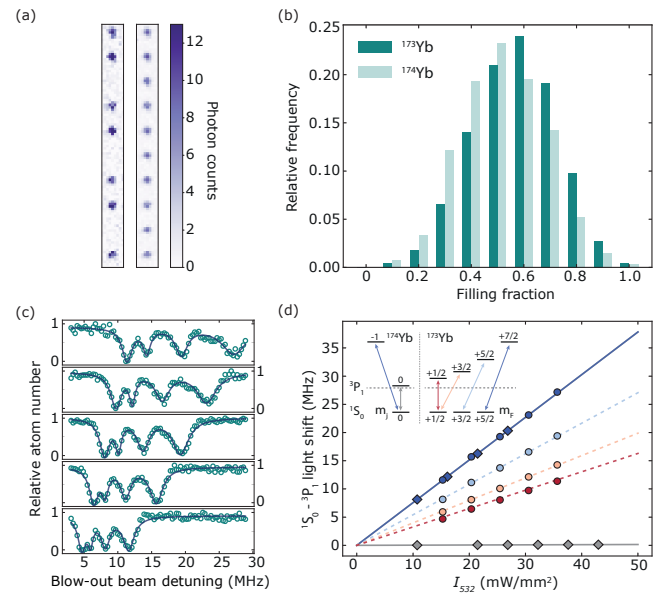


FIG. 4. Loading and imaging of ^{173}Yb arrays. (a) Single-shot and average of more than 2500 images of a 10-tweezer array of ^{173}Yb . The imaging pulse duration and intensity are set to 50 ms and $I_{399} \sim 10^{-2} I_s$, respectively. (b) Filling fraction of the tweezer array, obtained from over 2500 images for both ^{174}Yb and ^{173}Yb . A slight enhancement in the filling fraction for ^{173}Yb is noticeable, with an average of 58% compared to 50% for ^{174}Yb . (c) Blow-out spectroscopy of the $^1\text{S}_0 |F = 5/2) \rightarrow ^3\text{P}_1 |F' = 7/2)$ transition for tweezer-trapped ^{173}Yb atoms. The normalized atom number is plotted as a function of the blow-out pulse detuning from the free-space resonance, for varying tweezer trap depths [top to bottom: 1.8, 1.5, 1.3, 1.0, 0.8 mK]. The spectroscopic signal is fitted with a sum of four Lorentzian functions (solid lines) to determine the m'_F -dependent differential light shift. (d) Differential $^1\text{S}_0 - ^3\text{P}_1$ light shift for ^{174}Yb (diamonds) and ^{173}Yb (circles) as a function of the 532 nm tweezer peak intensity I_{532} . Solid lines are linear fits of the ^{174}Yb experimental data. Dashed lines are the predicted ^{173}Yb light shifts obtained from the measured ^{174}Yb light shifts (see text). The inset displays a scheme of the transitions associated to the measured light shifts with corresponding colors. Although all allowed transitions from each ground-state m_F sub-level are coupled by the blow-out pulse, only a few are depicted to avoid clutter. Grey dashed lines represent the free space energy of the excited states.

pulse duration of 50 ms and an imaging beam intensity $I_{399} \simeq 10^{-2} I_s$, where $I_s \simeq 60 \text{ mW/cm}^2$ is the saturation intensity of the $^1\text{S}_0 \rightarrow ^1\text{P}_1$ transition. Histograms in Fig. 4(b) show the single-atom loading probability distributions for ^{174}Yb and ^{173}Yb . We observe a slightly higher loading efficiency for ^{173}Yb , achieving a mean filling fraction $\simeq 58\%$, to be compared with $\simeq 50\%$ for ^{174}Yb . This suggests that for ^{173}Yb an enhanced loading mechanism is present [31, 33, 58, 59].

As our imaging scheme relies on narrow-line cooling, it would be advantageous to work under magic, i.e. state-independent, trapping conditions for the two states involved in the cooling transition [29, 30, 51]. In non-

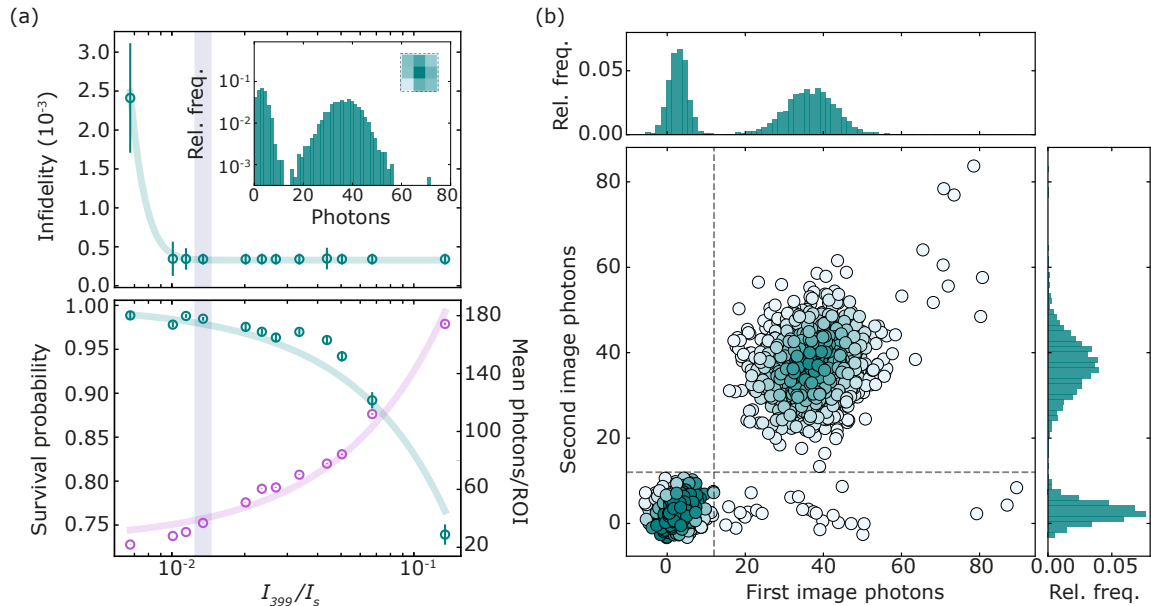


FIG. 5. Single-atom imaging of ^{173}Yb . (a) Imaging fidelity, survival probability and mean photon number per ROI as function of imaging beam intensity. Fidelity and survival probability data points are obtained from two consecutive imaging pulses of 50 ms duration, separated by 50 ms dark time. The vertical shaded line indicates the intensity at which 99.96(1)% fidelity, 98.5(2)% survival probability, and 36.8(1) mean photons/ROI are obtained. Shaded lines under the data are guides to the eye. The inset shows the photon count histogram for the first image, integrating over the 3x3 pixel ROIs centered at each trap. (b) Correlation between photon counts in the first and second images at the intensity marked by the shaded line in (a). The gray dashed lines indicate the photon count threshold which maximizes the global fidelity.

magic traps, a non-zero differential light shift is instead present between the two states, potentially compromising the effectiveness of narrow-line cooling: the frequency of the cooling transition depends the location of the atom within the trap and thus on the atom's energy. In addition, the transition frequency depends on the tweezer depth, and tweezer inhomogeneities across the array lead to reduced cooling performances. Linearly-polarized 532 nm traps were previously found to be magic for the $^1\text{S}_0 |J=0, m_J=0\rangle \rightarrow ^3\text{P}_1 |J'=1, m'_J=0\rangle$ transition of ^{174}Yb [29]. However, none of the corresponding $^1\text{S}_0 |F=5/2, m_F\rangle \rightarrow ^3\text{P}_1 |F'=F\pm 1, m'_F\rangle$ transitions in ^{173}Yb are predicted to feature a vanishing differential light shift at such wavelength.

To minimize array inhomogeneities, we apply a feedback protocol to our tweezer array [31], achieving an intensity inhomogeneity of less than 1.2% across a 10-trap array (see Appendix C for details). To characterize the trapping condition for ^{173}Yb , we measure the differential light-shift between the $^1\text{S}_0$ and $^3\text{P}_1$ states. To this aim, for both ^{174}Yb and ^{173}Yb , we perform spectroscopy with a green blow-out pulse (containing all polarizations) that expels atoms from the traps prior to imaging. Typical spectra of ^{173}Yb atoms are shown for different trapping intensities in Fig. 4(c), where the measured relative atom number is plotted as a function of the blow-out pulse detuning from the free-space $^1\text{S}_0 |F=5/2\rangle \rightarrow ^3\text{P}_1 |F'=7/2\rangle$ resonance. Here, the tweezer polarization is aligned along the quantization B

field, suppressing any vector light shift but not the tensor light shift, characterized by a $|m'_F|^2$ dependence [60]. We indeed observe four spectroscopic peaks corresponding to the different Zeeman sub-levels of the $^3\text{P}_1 |F'=7/2\rangle$ hyperfine state with $|m'_F|=1/2, 3/2, 5/2, 7/2$.

Figure 4(d) displays the differential light shift for each value of $|m'_F|$, obtained from Lorentzian fits of the blow-out spectra, as a function of the tweezer intensity. These are compared with the measured differential light shifts in ^{174}Yb . Through linear fits of the ^{174}Yb data, we estimate a differential light shift of $0.029(3)$ Hz cm 2 /W and $7.57(3)$ Hz cm 2 /W between the $^1\text{S}_0$ ground state and the $^3\text{P}_1 |J'=1, m'_J=0\rangle$ and $|J'=1, m'_J=\pm 1\rangle$ states, respectively. These values are consistent with Ref. 29, and are then used to determine the expected differential light shifts for ^{173}Yb sub-states, without relying on any *ab initio* polarizability model (see Appendix E). In brief, we express the light shift of each of the $^3\text{P}_1 |F'=7/2, m'_F\rangle$ states of ^{173}Yb as a weighted sum of the measured light shifts of the $^3\text{P}_1 |J'=1, m'_J=0, \pm 1\rangle$ states of ^{174}Yb , using the Clebsch-Gordan coefficients $|\langle F, m_F | J, m_J; I, m_I \rangle|^2$, with $F=7/2, J=1, I=5/2$ and $m_F=m_J+m_I$. We find that the measurements for ^{173}Yb are in good agreement with the predicted light shifts, confirming the validity of our simple approach. Linear fits of the ^{173}Yb data for $|m'_F|=7/2, 5/2, 3/2$, and $1/2$ yield differential light shifts of $7.58(9)$ Hz cm 2 /W, $5.49(6)$ Hz cm 2 /W, $4.07(3)$ Hz cm 2 /W, and $3.27(3)$ Hz cm 2 /W, respectively.

Comparing the predictions with the fitted values, we find a discrepancy of less than 2% for all states.

The complex internal structure of ^{173}Yb , arising from its high nuclear spin $I = 5/2$ and the associated differential light shifts, introduces challenges for single-atom imaging. We optimize the cooling beams detuning to address atoms in the $m_F = \pm 1/2$ states. Yet, the cooling efficiency decreases for higher- $|m_F|$ states due to the quadratic light shift experienced by states with $|m'_F| > 1/2$. In particular, atoms in the $m_F = \pm 5/2$ ground states are essentially dark to the green cooling light, owing to the several-MHz differential light shift of the $^3\text{P}_1 |F' = 7/2, m'_F = \pm 3/2, \pm 5/2, \pm 7/2\rangle$ states. Employing a two-color imaging scheme allows to overcome this potential issue, and yields high detection fidelities with limited atom loss. The blue light used for imaging acts indeed as a continuous repumper, redistributing the ground state population from the dark $m_F = \pm 5/2$ states into the bright $m_F = \pm 1/2, \pm 3/2$ states, thus improving the efficiency of green cooling. Moreover, the 5B MOT beams used as molasses feature a mix of polarizations that ensures m_F -symmetric optical pumping processes. Specifically, the horizontal beams are set to an intensity of $I_{\text{HOR}} \simeq 3 I_s$ and a detuning of -8.5 MHz from the $^3\text{P}_1 |F' = 7/2, m'_F = \pm 1/2\rangle$ states, while the vertical beam has an intensity of $I_{\text{VER}} \simeq 1.6 I_s$ and a detuning of -6.5 MHz from the same states.

In Fig. 5(a) we present the extracted array-averaged single-atom imaging infidelity and survival probability after a 50 ms imaging pulse, as a function of the imaging beam intensity. Each point is obtained from around 300 images of a 10-tweezer array. At the intensity indicated by the vertical shaded band, $I_{399} \simeq 1.3 \times 10^{-2} I_s$, we collect $36.8(1)$ photons per atom on average, resulting in a fidelity of $99.96(1)\%$ and a survival probability of $98.5(2)\%$. The inset presents a histogram of the photon counts in $3 \text{ px} \times 3 \text{ px}$ regions of interests (ROIs), where two peaks can be clearly distinguished, one corresponding to the background signal and the other to the single-atom signal. To characterize the imaging performances we acquire two successive images separated by 50 ms. Figure 5(b) shows the correlation between the photon counts in the first and second image for $I_{399} \simeq 1.3 \times 10^{-2} I_s$. For each value of the imaging intensity, we determine the global fidelity and survival probability following the optimization approach outlined in Ref. 61. The gray dashed lines in Fig. 5(b) represent the optimized photon-count thresholds that maximize the global fidelity. To obtain error bars for the fidelity and survival probability we employ a bootstrapping procedure [62]. We find that the imaging performance is optimized when the imaging beam is red-detuned by around -5 MHz from resonance. This helps to fine-tune the blue photon scattering rate at the low intensity used here, but may also be associated with sub-Doppler cooling effects from the retroreflected imaging beam itself [63].

IV. CONCLUSIONS

In this work, we have demonstrated high-fidelity and low-loss single-atom imaging of an ytterbium tweezer array loaded from a 5B MOT. We have shown that this MOT configuration allows to prepare cold and dense samples with short loading times for the most common ytterbium isotopes, making it a viable and practical solution for quantum science platforms employing high NA objective lenses. Despite its complex nuclear structure and our non-magic trapping wavelength, we have demonstrated the first high-fidelity single-atom imaging of ^{173}Yb atoms. Our two-color imaging scheme can be adapted to other fermionic alkaline-earth species, which lend themselves to high-dimensional quantum encodings exploiting their large and robust nuclear spin [64–66]. Moreover, the demonstrated single-atom detection scheme may be directly extended to quantum gas microscopes where, complemented by the nuclear spin-sensitive control of the metastable $^3\text{P}_0$ clock state, it will enable the investigation of two-orbital and/or $\text{SU}(N)$ -symmetric lattice models with single-particle resolution [16, 17, 24, 25, 67, 68].

ACKNOWLEDGMENTS

We thank M. Aidelsburger, N. Bruno, G. Cappellini, N. Darkwah Oppong, T. Höhn, G. Roati and L. Tarruell for useful discussions, and M. Marinelli for a careful reading of this manuscript. We also thank G. Brajnik, G. Cautero, A. Fondacaro, A. Martin, F. Salvador, A. Trenkwalder and the Instrumentation and Detectors Laboratory of Elettra Sincrotrone for technical support during the construction of the experimental apparatus, and F. Barbuio, G. Bartolini, G. Tazzoli, S. Vigneri, and J. Wang for participating in the initial setting up of the experiment. This work has received financial support from the European Research Council (ERC) under the European Union’s Horizon 2020 research and innovation programme (project OrbiDynaMIQs, GA No. 949438), and from the Italian MUR under the FARE 2020 programme (project FastOrbit, Prot. R20WNHFNKF). This work has also received funding from the European Union under the Horizon Europe program HORIZON-CL4-2022-QUANTUM-02-SGA (project PASQuanS2.1, GA no. 101113690), and by the Next Generation EU (Misione 4, Componente 1) under the MUR PRIN 2022 programme (project CoQuS, Prot. 2022ATM8FY) and the PNRR MUR project PE0000023-NQSTI.

Author contributions— O.A.K., A.M.F., R.P., W.L. and F.S. conceptualized the work and conducted the experiments. O.A.K. and A.M.F. analyzed the data and performed numerical simulations under the supervision of F.S.. O.A.K., A.M.F. and F.S. wrote the manuscript.

APPENDIX A: EXPERIMENTAL SEQUENCE

Our experimental apparatus is based on a commercial atomic source (AOSense Yb Beam RevC), featuring an integrated permanent magnet Zeeman slower (ZS) and a 2D MOT stage. A collimated hot ytterbium beam is generated by an oven kept at a temperature of 380°C, producing a flux of approximately 1.5×10^{12} atoms/s. The ZS is employed to reduce the longitudinal atomic beam velocity to approximately 40 m/s. The 2D MOT is utilized to cool atoms in the transversal direction and to deflect the beam towards an octagonal glass cell, where all experiments are performed. The typical experimental sequence employed for trapping and imaging single atoms in optical tweezers is illustrated in Fig. 6. The sequence begins by activating the 2D MOT and the slowing crossed beams (CBs, see main text) together with the green MOT beams and magnetic-field gradient to load the narrow-line MOT. After typically 200 ms of loading, the 2D MOT beams are turned off to prevent any residual flux from reaching the glass cell. Simultaneously the CBs are turned off while the ZS remains continuously on during the experiment. The MOT loading is followed by a two-stage compression lasting approximately 250 ms. In the first stage, referred to as pre-cMOT, the cloud is compressed at a slower rate, reaching a field gradient of 10 G/cm. During the subsequent cMOT phase, the quadrupole magnetic field is increased to about 30 G/cm over 100 ms as the MOT beams intensity and detuning are further reduced, reaching the minimum temperature. The following 50 ms are used to move the cloud over the tweezers position. The tweezers traps are turned on a few milliseconds before the pre-cMOT phase, with a typical trap depth of 2 mK. After the cMOT phase, the quadrupole magnetic field is switched off, and a 50 ms light-assisted collisions (LACs) pulse is applied to isolate single atoms in the tweezers. Imaging follows the LACs phase, with a typical duration of 50 ms.

APPENDIX B: FIVE-BEAM MOT SIMULATIONS

Monte Carlo simulations offer valuable insight into the working principle of the 5B MOT. Here, we present additional simulations beyond those in the main text to provide a more comprehensive overview of the 5B MOT operation. Figure 7(a) illustrates the trapped fraction in the MOT after 200 ms of time evolution as result of multiple simulated single-atom trajectories. Atoms are initialized at the intersection of the MOT beams, corresponding to the center of the quadrupole field, and evolve under the combined influence of the MOT beams, magnetic field gradient and gravity. We assume a textbook spin structure of the 1S_0 and 3P_1 states, such as in ^{174}Yb ($I = 0$). The simulation accounts only for losses arising from the atomic motion out of the trap, and it does not include e.g. background gas-induced or density-induced losses. Each trajectory is divided into steps of

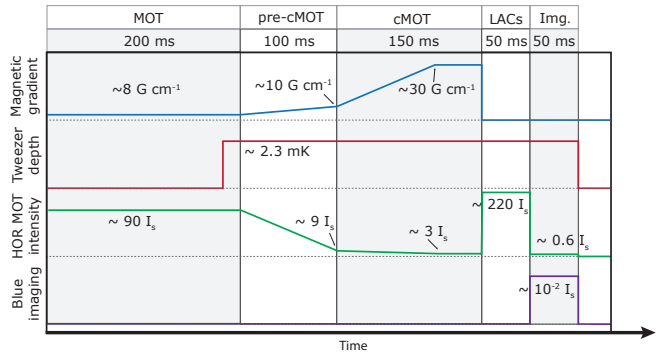


FIG. 6. Time diagram of the experimental sequence for trapping and imaging single ^{173}Yb atoms in optical tweezers. The sequence begins with a 200 ms MOT loading phase, followed by a 250 ms compression ramp, divided in two cMOT stages. The tweezers are turned on a few milliseconds before the first compression stage. After the cMOT is turned off, we apply a 50 ms LACs pulse to obtain single atoms in the tweezers. The two-color imaging typically lasts 50 ms.

duration $\tau = 1/\Gamma$, during which the atom can scatter a photon from one of the MOT beams. In particular, at each step we evaluate the scattering probability for each MOT beam as $P_i = \tau \cdot \Gamma_{sc,i}$, where $\Gamma_{sc,i}$ is the scattering rate of beam i and depends on the beam parameters as well as on the atomic position and velocity. For each beam independently, we stochastically determine if the scattering event is successful. If more than one beam yield a scattering event, we randomly choose one of them with uniform probability. After determining whether the atom has scattered a photon, and from which beam, we update its velocity taking into account absorption and isotropic spontaneous emission and evolve its coordinates with an equation of motion before proceeding to the next time step. For each data point in the figure, we simulate 100 trajectories and we determine the trapped fraction as the fraction of atoms in the MOT region at the end of the time evolution. We first investigate the interplay between the vertical and horizontal beams intensity, finding that the vertical beam requires significantly lower intensity than the horizontal beams. Moreover, we observe a correlation between the vertical and horizontal beams power: as the vertical beam power is changed from the optimal value, the MOT becomes less robust and requires less power in the horizontal beams. By fixing the horizontal beams intensity we also observe a correlation between the vertical beam parameters. In particular, we find that larger detunings require larger intensities to hold the atoms against gravity, as expected from the inverse dependence on detuning of the scattering force. The optimal working point obtained in simulations is in agreement with experimental results for ^{171}Yb shown in Fig. 2(a) except for a small difference in the intensity of the vertical beam. We attribute this difference to the internal structure of the fermionic isotope, which is not accounted for in our simulations. In Fig. 7(b),

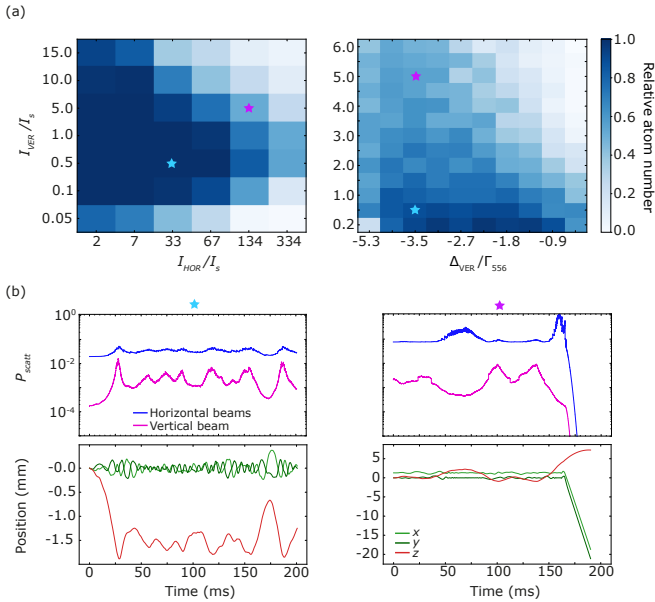


FIG. 7. Monte Carlo simulations of the five-beam MOT. (a) Fraction of atoms trapped in the MOT as a function of the vertical and horizontal beam intensities and the vertical beam detuning. Atoms are initialized at the intersection of the MOT beams, corresponding to the center of the quadrupole field, with zero velocity. An atom is considered trapped if it is retained in the MOT region after 200 ms of time evolution. Each point is obtained from 100 individual trajectories. The cyan and purple stars indicate representative points of the 5B MOT operation, corresponding to high and low MOT stability respectively. (b) Illustrative scattering probability (top) and associated atomic trajectory (bottom) as a function of time for the two scenarios marked by stars in panel (a). Blue (magenta) curves represent the probability of scattering from any of the horizontal beams (the vertical beam) during the simulation. For the first condition (cyan star), where the trapped fraction is maximized, the atom experiences repeated bounces in the vertical direction caused by sudden variations in the vertical beam scattering probability. For the second condition (purple star), where intensities are higher and the trapped fraction is lower, the atom is pushed upward by the vertical beam and eventually escapes horizontally after approximately 100 ms.

we present two illustrative trajectories to provide insight into the results shown in Fig. 7(a). In particular we show the scattering probability from the horizontal and vertical beams, along with the atom position as a function of time, for two representative simulation scenarios: one where the captured fraction is maximized and another one where it is around 50%. For the first one, the scattering probability from the vertical beam is generally much lower than that of the horizontal beams, which can be attributed to lower power broadening of the transition compared to the more intense horizontal beams. Indeed, the atoms do not scatter many photons from the vertical beam until the resonant condition is matched. This is marked by a peak in the scattering probability and a sudden inversion of motion along the vertical direction. This

results in the peculiar shape of the atomic vertical trajectory, characterized by a series of free falls and bounces which keep the atoms inside the MOT region. When the vertical intensity is too high, atoms have a higher probability of escaping. As visible from the second trajectory, this occurs because the atom is pushed upward by the vertical beam until it enters a region of the magnetic quadrupole field where horizontal confinement is less robust. Lowering the horizontal beam power in this case is beneficial, as it reduces the horizontal scattering rate, giving the atom more time to fall back in a more stable region of the MOT before scattering from the horizontal beams.

APPENDIX C: TWEEZER ARRAY HOMOGENIZATION

Imaging performances are sensitive to amplitude inhomogeneities across the tweezer array. Inhomogeneities introduce variations in the $^1\text{S}_0 - ^3\text{P}_1$ differential light shift, leading to a reduced cooling efficiency in our imaging protocol. To achieve uniform trapping across the array, we apply two amplitude homogenization steps, similarly to the method described in Ref. 31. In the first step, we acquire an image of the optical tweezer array using a CMOS camera (Zelux CS165MU) and fit the image with a sum of Gaussian functions. For each tweezer we determine an error, defined as:

$$E_i = \frac{I_i - \langle I \rangle}{\langle I \rangle} \quad (\text{C1})$$

where I_i is proportional to the intensity of each tweezer and $\langle I \rangle$ is the average of the I_i values. The amplitudes A_i of the new RF tones driving the AOD are obtained by taking the difference between the old RF array and the retrieved error, adding a proportional gain:

$$A_i^{\text{new}} = A_i^{\text{old}} - pE_i \quad (\text{C2})$$

The feedback loop is iterated until the amplitude homogeneity converges to a stationary and satisfactory level. We can perform this feedback protocol either imaging the tweezers produced by the microscope objective at the atomic plane, or the intermediate tweezers produced by the scan lens (see scheme in Fig. 8 (a)). Imaging the tweezers at the atomic plane, yields a remarkably low coefficient of variation (CV) of 1.4% across an array of 40 tweezers spaced by $1.3\ \mu\text{m}$ after 14 iterations, as shown in Fig. 8(a). However, directly imaging the tweezers at the atom plane is not always practical. Therefore, we implement the feedback loop at the scan lens focal plane, upstream of the tube lens and the objective. At this stage, the feedback loop corrects for inhomogeneities arising from nonlinearities in the AOD crystal and RF amplifier. While this approach improves the uniformity at the

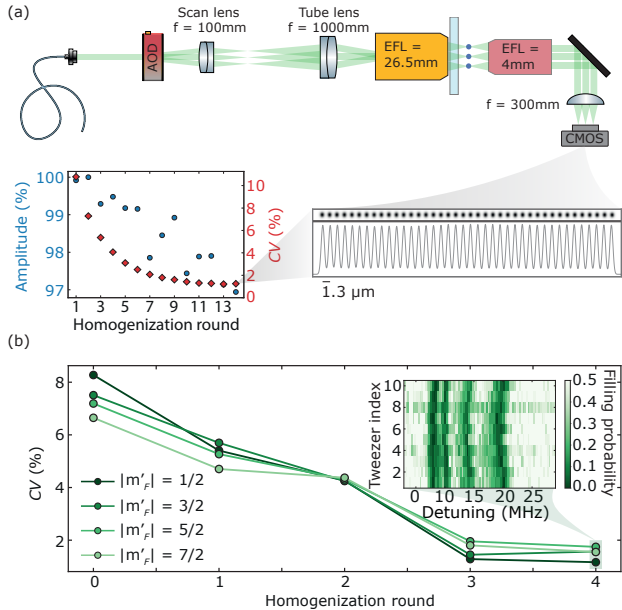


FIG. 8. Tweezer amplitude homogenization. (a) Optical tweezers are produced using an AOD. The intermediate tweezers, generated using a scan lens with $f = 100$ mm, are imaged onto the atomic plane through a tube lens with $f = 1000$ mm and the microscope objective. The intensity distribution of each tweezer trap at the atom plane is measured using another objective with $\text{EFL} = 4$ mm and a tube lens with $f = 300$ mm, focusing on a CMOS camera. The plot shows the mean amplitude and coefficient of variation (CV) across a 40-tweezer array, spaced by $1.3 \mu\text{m}$, as a function of feedback iterations. The CV reaches 1.4% after 14 iterations. The inset shows the image and the fit of the tweezer array after the final homogenization step. (b) Differential light shifts throughout the tweezer array are measured via blow-out spectroscopy and used to correct amplitude inhomogeneities. The plot shows the CV as a function of iteration round for a 10-tweezer array with $\sim 8 \mu\text{m}$ spacing. The inset shows the blow-out spectroscopy results after the final homogenization round.

scan lens plane, it does not account for aberrations introduced by downstream optics, and thus does not guarantee optimal uniformity at the atom plane. Nonetheless, following the homogenization, we measure a CV of 5% at the atom plane, making a significant improvement from the initial CV of 11%. To further reduce the CV, we apply a second homogenization procedure that leverages light shifts in non-magic traps to finely compensate any remaining inhomogeneities.

To this end, we exploit the differential light shifts induced on the $^1\text{S}_0 \rightarrow ^3\text{P}_1$ transition by the 532 nm trapping light for ^{173}Yb . We apply a similar amplitude homogenization protocol as before, but use the atomic light shift as the figure of merit in this case. To measure the light shifts we perform blow-out spectroscopy on the $^1\text{S}_0 \rightarrow ^3\text{P}_1$ transition using a green pulse to expel atoms from the trap, followed by a blue imaging pulse. The blow-out pulse is linearly polarized at 45° with respect to the quantization axis, allowing excitation of both

the π and σ^\pm transitions. This allows us to resolve four distinct transitions connecting the $^1\text{S}_0 |m_F\rangle$ states to the $^3\text{P}_1 |m'_F = \pm 1/2, \pm 3/2, \pm 5/2, \pm 7/2\rangle$ states. By measuring the differential light shift in each tweezer, we can adjust the AOD driving RF tone amplitudes to correct for inhomogeneities. In Fig. 8(b), we show the homogenization results, plotting the CV of the differential light shift for the different tweezers. We achieve a CV of 1.1% for the $^1\text{S}_0 \rightarrow ^3\text{P}_1 |F' = 7/2, m'_F = \pm 1/2\rangle$ transitions, which are the ones we address for molasses cooling during imaging. The inset of Fig. 8(b) shows the results of the blow-out spectroscopy performed after the final round of homogenization.

APPENDIX D: TWEEZER WAIST CHARACTERIZATION

A crucial parameter to characterize an optical tweezer trap is the trap frequency. We determine the tweezer trap frequencies using the parametric heating technique [69]. This method relies on periodically modulating the trap depth to induce atom losses, which are maximized when the modulation frequency is twice the trapping frequency. We begin by loading a ten-site optical tweezer array at a trap depth of 2 mK and take a low-loss initial image. The trap depth is then lowered to about 1 mK to enhance atom loss, followed by amplitude modulation for 100 ms. After modulation, the trap depth is ramped back to 2 mK, and a second image is taken to count the remaining atoms. The frequency spectrum reveals two distinct resonances, corresponding to the axial and radial trap frequencies. The presence of a single radial resonance indicates the absence of astigmatism in the optical tweezer traps. From the measured trap frequencies, we indirectly determine the tweezer waist by expressing it in terms of the ratio of the radial to axial trap frequencies. This approach removes dependence on the trap depth, allowing the tweezer waist to be written as:

$$w_0 = \frac{\lambda}{\pi\sqrt{2}} \frac{\omega_r}{\omega_z} \quad (\text{D1})$$

Using this relation along with the experimentally measured radial and axial trap frequencies, we determine the tweezer waist to be: $w_0 = 578(4)$ nm. This value is obtained after correcting misalignments of the objective lens relative to the glass cell, which introduce aberrations and lead to a reduction in both the trap depth and trap frequencies. To this end, we adjust the objective tilt in order to maximize the axial trap frequency measured with parametric heating.

APPENDIX E: POLARIZABILITY CALCULATIONS

The optical potential experienced by an atom is determined by the product of the state-dependent polarizabil-

ity and the intensity profile of the trap:

$$U(\mathbf{r}) = -\frac{1}{2\epsilon_0 c} \alpha(\omega) I(\mathbf{r}) \quad (\text{E1})$$

The polarizability α is obtained from second-order perturbation theory [70]:

$$\alpha(\omega) = \sum_f \frac{2\omega_{if} |\langle i | \mathbf{\epsilon} \cdot \mathbf{d} | f \rangle|^2}{\hbar(\omega_{if}^2 - \omega^2)} \quad (\text{E2})$$

where \mathbf{d} is the dipole operator that connects the atomic level of interest $|i\rangle$ to upper atomic levels $|f\rangle$, $\mathbf{\epsilon}$ is the polarization of the light and $\hbar\omega_{if}$ is the energy difference between the state $|i\rangle$ and the states $|f\rangle$. The polarizability operator for an atomic state $|i\rangle$ can be expressed as a Cartesian tensor, represented as [60]:

$$\hat{\alpha}_{\mu\nu}(\omega) = \sum_f \frac{2\omega_{if}}{\hbar(\omega_{if}^2 - \omega^2)} \langle i | \hat{d}_\mu | f \rangle \langle f | \hat{d}_\nu | i \rangle \quad (\text{E3})$$

To relate the transition dipole moments to experimentally measured lifetimes, we use the Wigner-Eckart theorem, which allows to express the dipole moment as the product between a scalar quantity, i.e. the so-called reduced matrix element, and the Clebsch-Gordan coefficients [60]:

$$\begin{aligned} \langle n, J, m_J | \hat{d}_q | n', J', m'_J \rangle = \\ = \langle n, J | \hat{d} | n', J' \rangle (-1)^{J'-1-m_J} \sqrt{2J+1} \begin{pmatrix} 1 & J' & J \\ q & m'_J & -m_J \end{pmatrix} \end{aligned} \quad (\text{E4})$$

where the quantum number n labels the electronic configuration, J is the total electronic angular momentum and m_J is the angular momentum projection along the quantization axis. The polarization of the light is defined by the index q , with $q = \pm 1$ corresponding to right- and left-circular polarization, respectively, and $q = 0$ to linear polarization along the quantization axis. The term in parenthesis is the Wigner 3-j symbol. The reduced matrix element $\langle n, J | \hat{d} | n', J' \rangle$ can be related to the decay rate of the nJ' states:

$$\Gamma_{n'J',nJ} = \frac{\omega_{n'J'nJ}^3}{3\pi\hbar c^3\epsilon_0} \frac{|\langle n, J | \hat{d} | n', J' \rangle|^2}{2J'+1}$$

where $\omega_{n'J'nJ}$ is the transition angular frequency. This approach allows us to determine the $|m_J|$ state-dependent polarizability from the measured lifetimes of states with electronic quantum number n' and total electronic angular momentum J' . We apply this method

to calculate the polarizability of the ${}^1\text{S}_0 |J = 0, m_J = 0\rangle$ and ${}^3\text{P}_1 |J = 1, m_J = 0, \pm 1\rangle$ states of ${}^{174}\text{Yb}$. This model does not account for any hyperfine structure, and is thus valid for $I = 0$. The latter however becomes important for fermionic isotopes, where $I \neq 0$ and the total atomic angular momentum $F \neq J$.

To extend our model to fermionic isotopes, and in particular to ${}^{173}\text{Yb}$, we follow a simple approach. Since the $|F, m_F\rangle$ states are given by superpositions of $|J, m_J; I, m_I\rangle$ states, whose amplitudes are the Clebsch-Gordan coefficients $\langle F, m_F | J, m_J; I, m_I \rangle$, we can express the polarizability $\alpha_{|m_F\rangle}$ of the ${}^3\text{P}_1 |F = 7/2, m_F\rangle$ states of ${}^{173}\text{Yb}$ as:

$$\begin{aligned} \alpha_{|m_F=\pm 7/2\rangle} &= \alpha_{|m_J=\pm 1\rangle} \\ \alpha_{|m_F=\pm 5/2\rangle} &= \frac{5}{7} \alpha_{|m_J=\pm 1\rangle} + \frac{2}{7} \alpha_{|m_J=0\rangle} \\ \alpha_{|m_F=\pm 3/2\rangle} &= \frac{11}{21} \alpha_{|m_J=\pm 1\rangle} + \frac{10}{21} \alpha_{|m_J=0\rangle} \\ \alpha_{|m_F=\pm 1/2\rangle} &= \frac{3}{7} \alpha_{|m_J=\pm 1\rangle} + \frac{4}{7} \alpha_{|m_J=0\rangle} \end{aligned} \quad (\text{E5})$$

where $\alpha_{|m_J\rangle}$ is the polarizability of the ${}^3\text{P}_1 |J = 1, m_J\rangle$ state of ${}^{174}\text{Yb}$. We thus extend our polarizability model to fermionic isotopes without explicitly including the total atomic angular momentum F and its projection m_F in the calculation of the dipole matrix elements. Thereby, we can predict the light shifts of the ${}^{173}\text{Yb}$ ${}^3\text{P}_1 |F = 7/2, m_F\rangle$ states based on the measured light shifts of the ${}^{174}\text{Yb}$ ${}^3\text{P}_1 |J = 1, m_J\rangle$ states [see Fig. 4(d)].

In our model, the polarizabilities of the ${}^1\text{S}_0$, ${}^3\text{P}_1$, and ${}^3\text{P}_0$ states are corrected to match known constraints. In particular, the asymptotic value of the ${}^1\text{S}_0$ state polarizability is reduced by $-1.4 \text{ Hz cm}^2/\text{W}$ to align with the static polarizability value calculated in [71]. To match the experimentally determined magic wavelength of 532 nm for the ${}^1\text{S}_0 |J = 0, m_J = 0\rangle \rightarrow {}^3\text{P}_1 |J' = 1, m'_J = 0\rangle$ transition in ${}^{174}\text{Yb}$, a small offset of $-0.15 \text{ Hz cm}^2/\text{W}$ is applied to the polarizability of the ${}^3\text{P}_1$ state. This adjustment also predicts additional magic wavelengths, including 487 nm for the ${}^3\text{P}_1 |F = 3/2, |m_F| = 1/2\rangle$ state in ${}^{171}\text{Yb}$, which is experimentally measured in [32]. With these corrections, we find that the differential light shift between the ${}^1\text{S}_0 |J = 0, m_J = 0\rangle$ and ${}^3\text{P}_1 |J' = 1, m'_J = \pm 1\rangle$ states of ${}^{174}\text{Yb}$ lies within 20% from our experimental measurements. This remaining discrepancy likely arises from inaccuracies in the tweezer waist estimation and power calibration.

[1] A. V. Gorshkov, A. M. Rey, A. J. Daley, M. M. Boyd, J. Ye, P. Zoller, and M. D. Lukin, *Alkaline-Earth-Metal*

Atoms as Few-Qubit Quantum Registers, *Phys. Rev. Lett.* **102**, 110503 (2009).

[2] K. Shibata, S. Kato, A. Yamaguchi, S. Uetake, and Y. Takahashi, *A scalable quantum computer with ultra-narrow optical transition of ultracold neutral atoms in an optical lattice*, *Appl. Phys. B* **97**, 753 (2009).

[3] A. J. Daley, *Quantum computing and quantum simulation with group-II atoms*, *Quant. Inf. Proc.* **10**, 865 (2011).

[4] G. Pagano, F. Scazza, and M. Foss-Feig, *Fast and Scalable Quantum Information Processing with Two-Electron Atoms in Optical Tweezer Arrays*, *Adv. Quantum Tech.* **2**, 1800067 (2019).

[5] I. S. Madjarov, J. P. Covey, A. L. Shaw, J. Choi, A. Kale, A. Cooper, H. Pichler, V. Schkolnik, J. R. Williams, and M. Endres, *High-fidelity entanglement and detection of alkaline-earth Rydberg atoms*, *Nat. Phys.* **16**, 857 (2020).

[6] Y. Wu, S. Kolkowitz, S. Puri, and J. D. Thompson, *Erasure conversion for fault-tolerant quantum computing in alkaline earth Rydberg atom arrays*, *Nat. Comm.* **13**, 4657 (2022).

[7] N. Chen, L. Li, W. Huie, M. Zhao, I. Vetter, C. H. Greene, and J. P. Covey, *Analyzing the Rydberg-based optical-metastable-ground architecture for ^{171}Yb nuclear spins*, *Phys. Rev. A* **105**, 052438 (2022).

[8] K. Sahay, J. Jin, J. Claes, J. D. Thompson, and S. Puri, *High-Threshold Codes for Neutral-Atom Qubits with Biased Erasure Errors*, *Phys. Rev. X* **13**, 041013 (2023).

[9] Z. Jia, W. Huie, L. Li, W. K. C. Sun, X. Hu, Aakash, H. Kogan, A. Karve, J. Y. Lee, and J. P. Covey, *An architecture for two-qubit encoding in neutral ytterbium-171 atoms*, *npj Quantum Inf.* **10**, 106 (2024).

[10] A. D. Ludlow, M. M. Boyd, J. Ye, E. Peik, and P. O. Schmidt, *Optical atomic clocks*, *Rev. Mod. Phys.* **87**, 637 (2015).

[11] W. F. McGrew, X. Zhang, R. J. Fasano, S. A. Schäffer, K. Beloy, D. Nicolodi, R. C. Brown, N. Hinkley, G. Milani, M. Schioppo, T. H. Yoon, and A. D. Ludlow, *Atomic clock performance enabling geodesy below the centimetre level*, *Nature* **564**, 87 (2018).

[12] E. Oelker, R. B. Hutson, C. J. Kennedy, L. Sonderhouse, T. Bothwell, A. Goban, D. Kedar, C. Sanner, J. M. Robinson, G. E. Marti, D. G. Matei, T. Legero, M. Giunta, R. Holzwarth, F. Riehle, U. Sterr, and J. Ye, *Demonstration of 4.8×10^{-17} stability at 1 s for two independent optical clocks*, *Nat. Photonics* **13**, 714 (2019).

[13] X. Zheng, J. Dolde, V. Lochab, B. N. Merriman, H. Li, and S. Kolkowitz, *Differential clock comparisons with a multiplexed optical lattice clock*, *Nature* **602**, 425 (2022).

[14] L. Hu, N. Poli, L. Salvi, and G. M. Tino, *Atom Interferometry with the Sr Optical Clock Transition*, *Phys. Rev. Lett.* **119**, 263601 (2017).

[15] J. Rudolph, T. Wilkason, M. Nantel, H. Swan, C. M. Holland, Y. Jiang, B. E. Garber, S. P. Carman, and J. M. Hogan, *Large Momentum Transfer Clock Atom Interferometry on the 689 nm Intercombination Line of Strontium*, *Phys. Rev. Lett.* **124**, 083604 (2020).

[16] A. V. Gorshkov, M. Hermele, V. Gurarie, C. Xu, P. S. Julienne, J. Ye, P. Zoller, E. Demler, M. D. Lukin, and A. M. Rey, *Two-orbital $SU(N)$ magnetism with ultracold alkaline-earth atoms*, *Nat. Phys.* **6** (2010), 10.1038/nphys1535.

[17] M. A. Cazalilla and A. M. Rey, *Ultracold Fermi gases with emergent $SU(N)$ symmetry*, *Reports on Progress in Physics* **77**, 124401 (2014).

[18] R. Zhang, Y. Cheng, P. Zhang, and H. Zhai, *Controlling the interaction of ultracold alkaline-earth atoms*, *Nat. Rev. Phys.* **2**, 213 (2020).

[19] F. M. Surace, P. Fromholz, N. D. Oppong, M. Dalmonte, and M. Aidelsburger, *Ab Initio Derivation of Lattice-Gauge-Theory Dynamics for Cold Gases in Optical Lattices*, *PRX Quantum* **4**, 020330 (2023).

[20] F. M. Surace, P. Fromholz, F. Scazza, and M. Dalmonte, *Scalable, ab initio protocol for quantum simulating $SU(N) \times U(1)$ Lattice Gauge Theories*, *Quantum* **8**, 1359 (2024).

[21] F. Scazza, C. Hofrichter, M. Höfer, P. C. De Groot, I. Bloch, and S. Fölling, *Observation of two-orbital spin-exchange interactions with ultracold $SU(N)$ -symmetric fermions*, *Nature Phys.* **10**, 779 (2014).

[22] X. Zhang, M. Bishof, S. L. Bromley, C. V. Kraus, M. S. Safronova, P. Zoller, A. M. Rey, and J. Ye, *Spectroscopic observation of $SU(N)$ -symmetric interactions in Sr orbital magnetism*, *Science* **345**, 1467 (2014).

[23] G. Cappellini, M. Mancini, G. Pagano, P. Lombardi, L. Livi, M. Siciliani de Cumis, P. Cancio, M. Pizzocaro, D. Calonico, F. Levi, C. Sias, J. Catani, M. Inguscio, and L. Fallani, *Direct Observation of Coherent Interorbital Spin-Exchange Dynamics*, *Phys. Rev. Lett.* **113**, 120402 (2014).

[24] L. Rieger, N. Darkwah Oppong, M. Höfer, D. R. Fernandes, I. Bloch, and S. Fölling, *Localized Magnetic Moments with Tunable Spin Exchange in a Gas of Ultracold Fermions*, *Phys. Rev. Lett.* **120**, 143601 (2018).

[25] M. Kanász-Nagy, Y. Ashida, T. Shi, C. P. Moca, T. N. Ikeda, S. Fölling, J. I. Cirac, G. Zaránd, and E. A. Demler, *Exploring the anisotropic Kondo model in and out of equilibrium with alkaline-earth atoms*, *Phys. Rev. B* **97**, 155156 (2018).

[26] B. Abeln, K. Sponselee, M. Diem, N. Pintul, K. Sengstock, and C. Becker, *Interorbital interactions in an $SU(2) \times SU(6)$ -symmetric Fermi-Fermi mixture*, *Phys. Rev. A* **103**, 033315 (2021).

[27] A. Cooper, J. P. Covey, I. S. Madjarov, S. G. Porsev, M. S. Safronova, and M. Endres, *Alkaline-Earth Atoms in Optical Tweezers*, *Phys. Rev. X* **8**, 041055 (2018).

[28] M. A. Norcia, A. W. Young, and A. M. Kaufman, *Microscopic Control and Detection of Ultracold Strontium in Optical-Tweezer Arrays*, *Phys. Rev. X* **8**, 041054 (2018).

[29] S. Saskin, J. T. Wilson, B. Grinkemeyer, and J. D. Thompson, *Narrow-Line Cooling and Imaging of Ytterbium Atoms in an Optical Tweezer Array*, *Phys. Rev. Lett.* **122**, 143002 (2019).

[30] J. P. Covey, I. S. Madjarov, A. Cooper, and M. Endres, *2000-Times Repeated Imaging of Strontium Atoms in Clock-Magic Tweezer Arrays*, *Phys. Rev. Lett.* **122**, 173201 (2019).

[31] A. Jenkins, J. W. Lis, A. Senoo, W. F. McGrew, and A. M. Kaufman, *Ytterbium Nuclear-Spin Qubits in an Optical Tweezer Array*, *Phys. Rev. X* **12**, 021027 (2022).

[32] S. Ma, A. P. Burgers, G. Liu, J. Wilson, B. Zhang, and J. D. Thompson, *Universal Gate Operations on Nuclear Spin Qubits in an Optical Tweezer Array of ^{171}Yb Atoms*, *Phys. Rev. X* **12**, 021028 (2022).

[33] W. Huie, L. Li, N. Chen, X. Hu, Z. Jia, W. K. C. Sun, and J. P. Covey, *Repetitive Readout and Real-Time Control of Nuclear Spin Qubits in ^{171}Yb Atoms*, *PRX Quantum* **4**, 030337 (2023).

[34] M. A. Norcia, W. B. Cairncross, K. Barnes, P. Battaglino, A. Brown, M. O. Brown, K. Cassella, C.-A. Chen, R. Coxe, D. Crow, J. Epstein, C. Griger,

A. M. W. Jones, H. Kim, J. M. Kindem, J. King, S. S. Kondov, K. Kotru, J. Lauigan, M. Li, M. Lu, E. Megidish, J. Marjanovic, M. McDonald, T. Mittiga, J. A. Muniz, S. Narayanaswami, C. Nishiguchi, R. Notermans, T. Paule, K. A. Pawlak, L. S. Peng, A. Ryou, A. Smull, D. Stack, M. Stone, A. Sucich, M. Urbanek, R. J. M. van de Veerdonk, Z. Vendeiro, T. Wilkason, T.-Y. Wu, X. Xie, X. Zhang, and B. J. Bloom, *Midcircuit Qubit Measurement and Rearrangement in a ^{171}Yb Atomic Array*, *Phys. Rev. X* **13**, 041034 (2023).

[35] Y. Nakamura, T. Kusano, R. Yokoyama, K. Saito, K. Higashi, N. Ozawa, T. Takano, Y. Takasu, and Y. Takahashi, *Hybrid Atom Tweezer Array of Nuclear Spin and Optical Clock Qubits*, *Phys. Rev. X* **14**, 041062 (2024).

[36] R. Tao, M. Ammenwerth, F. Gyger, I. Bloch, and J. Zeiher, *High-Fidelity Detection of Large-Scale Atom Arrays in an Optical Lattice*, *Phys. Rev. Lett.* **133**, 013401 (2024).

[37] S. Ma, G. Liu, P. Peng, B. Zhang, S. Jandura, J. Claes, A. P. Burgers, G. Pupillo, S. Puri, and J. D. Thompson, *High-fidelity gates and mid-circuit erasure conversion in an atomic qubit*, *Nature* **622**, 279 (2023).

[38] P. Scholl, A. L. Shaw, R. B.-S. Tsai, R. Finkelstein, J. Choi, and M. Endres, *Erasure conversion in a high-fidelity Rydberg quantum simulator*, *Nature* **622**, 273 (2023).

[39] J. W. Lis, A. Senoo, W. F. McGrew, F. Rönchen, A. Jenkins, and A. M. Kaufman, *Midcircuit Operations Using the omg Architecture in Neutral Atom Arrays*, *Phys. Rev. X* **13**, 041035 (2023).

[40] I. S. Madjarov, A. Cooper, A. L. Shaw, J. P. Covey, V. Schkolnik, T. H. Yoon, J. R. Williams, and M. Endres, *An Atomic-Array Optical Clock with Single-Atom Readout*, *Phys. Rev. X* **9**, 041052 (2019).

[41] M. A. Norcia, A. W. Young, W. J. Eckner, E. Oelker, J. Ye, and A. M. Kaufman, *Seconds-scale coherence on an optical clock transition in a tweezer array*, *Science* **366**, 93 (2019).

[42] A. W. Young, W. J. Eckner, W. R. Milner, D. Kedar, M. A. Norcia, E. Oelker, N. Schine, J. Ye, and A. M. Kaufman, *Half-minute-scale atomic coherence and high relative stability in a tweezer clock*, *Nature* **588**, 408 (2020).

[43] A. Cao, W. J. Eckner, T. Lukin Yelin, A. W. Young, S. Jandura, L. Yan, K. Kim, G. Pupillo, J. Ye, N. Darkwah Oppong, and A. M. Kaufman, *Multi-qubit gates and Schrödinger cat states in an optical clock*, *Nature* **634**, 315 (2024).

[44] A. L. Shaw, R. Finkelstein, R. B.-S. Tsai, P. Scholl, T. H. Yoon, J. Choi, and M. Endres, *Multi-ensemble metrology by programming local rotations with atom movements*, *Nat. Phys.* **20**, 195 (2024).

[45] R. Finkelstein, R. B.-S. Tsai, X. Sun, P. Scholl, S. Direkci, T. Gefen, J. Choi, A. L. Shaw, and M. Endres, *Universal quantum operations and ancilla-based read-out for tweezer clocks*, *Nature* **634**, 321 (2024).

[46] C. Gross and I. Bloch, *Quantum simulations with ultracold atoms in optical lattices*, *Science* **357**, 995 (2017).

[47] A. Browaeys and T. Lahaye, *Many-body physics with individually controlled Rydberg atoms*, *Nat. Phys.* **16**, 132 (2020).

[48] A. M. Kaufman and K.-K. Ni, *Quantum science with optical tweezer arrays of ultracold atoms and molecules*, *Nat. Phys.* **17**, 1324 (2021).

[49] P. Ilzhöfer, G. Durastante, A. Patscheider, A. Trautmann, M. J. Mark, and F. Ferlaino, *Two-species five-beam magneto-optical trap for erbium and dysprosium*, *Phys. Rev. A* **97**, 023633 (2018).

[50] D. S. Grün, S. J. M. White, A. Ortú, A. Di Carli, H. Edri, M. Lepers, M. J. Mark, and F. Ferlaino, *Optical Tweezer Arrays of Erbium Atoms*, *Phys. Rev. Lett.* **133**, 223402 (2024).

[51] R. Yamamoto, J. Kobayashi, T. Kuno, K. Kato, and Y. Takahashi, *An ytterbium quantum gas microscope with narrow-line laser cooling*, *New J. Phys.* **18**, 023016 (2016).

[52] A. Urech, I. H. A. Knottnerus, R. J. C. Spreeuw, and F. Schreck, *Narrow-line imaging of single strontium atoms in shallow optical tweezers*, *Phys. Rev. Res.* **4**, 023245 (2022).

[53] B. Plotkin-Swing, A. Wirth, D. Gochnauer, T. Rahman, K. E. McAlpine, and S. Gupta, *Crossed-beam slowing to enhance narrow-line ytterbium magneto-optic traps*, *Rev. Sci. Instr.* **91**, 093201 (2020).

[54] W. Lunden, L. Du, M. Cantara, P. Barral, A. O. Jamison, and W. Ketterle, *Enhancing the capture velocity of a Dy magneto-optical trap with two-stage slowing*, *Phys. Rev. A* **101**, 063403 (2020).

[55] B. Seo, P. Chen, Z. Chen, W. Yuan, M. Huang, S. Du, and G.-B. Jo, *Efficient production of a narrow-line erbium magneto-optical trap with two-stage slowing*, *Phys. Rev. A* **102**, 013319 (2020).

[56] Fluctuations of the radiation force from the vertical upward beam are enhanced by the optical pumping processes within the large nuclear spin structure of ^{173}Yb , where the transitions associated with each nuclear spin state of the ground manifold feature widely different line strengths.

[57] R. Maruyama, R. H. Wynar, M. V. Romalis, A. Andalkar, M. D. Swallows, C. E. Pearson, and E. N. Fortson, *Investigation of sub-Doppler cooling in an ytterbium magneto-optical trap*, *Phys. Rev. A* **68**, 011403 (2003).

[58] T. Grunzweig, A. Hilliard, M. McGovern, and M. Andersen, *Near-deterministic preparation of a single atom in an optical microtrap*, *Nat. Phys.* **6**, 951 (2011).

[59] M. O. Brown, T. Thiele, C. Kiehl, T.-W. Hsu, and C. A. Regal, *Gray-Molasses Optical-Tweezer Loading: Controlling Collisions for Scaling Atom-Array Assembly*, *Phys. Rev. X* **9**, 011057 (2019).

[60] D. A. Steck, *Quantum and Atom Optics*, <https://atomoptics.uoregon.edu/~dsteck/teaching/quantum-optics/>.

[61] A. Holman, Y. Xu, X. Sun, J. Wu, M. Wang, B. Seo, N. Yu, and S. Will, *Trapping of Single Atoms in Metasurface Optical Tweezer Arrays*, [arXiv:2411.05321](https://arxiv.org/abs/2411.05321).

[62] C. M. Holland, Y. Lu, and L. W. Cheuk, *Bichromatic Imaging of Single Molecules in an Optical Tweezer Array*, *Phys. Rev. Lett.* **131**, 053202 (2023).

[63] N. Kostylev, E. Ivanov, M. E. Tobar, and J. J. McFerran, *Sub-Doppler cooling of ytterbium with the $1S0\#x2013;1P1$ transition including 171Yb ($I=1/2$)*, *J. Opt. Soc. Am. B* **31**, 1614 (2014).

[64] S. Omanakuttan, A. Mitra, M. J. Martin, and I. H. Deutsch, *Quantum optimal control of ten-level nuclear spin qudits in ^{87}Sr* , *Phys. Rev. A* **104**, L060401 (2021).

[65] D. González-Cuadra, T. V. Zache, J. Carrasco, B. Kraus, and P. Zoller, *Hardware Efficient Quantum Simulation of Non-Abelian Gauge Theories with Qudits on Rydberg*

Platforms, *Phys. Rev. Lett.* **129**, 160501 (2022).

[66] H. Ahmed, A. Litvinov, P. Guesdon, E. Maréchal, J. H. Huckans, B. Pasquiou, B. Laburthe-Tolra, and M. R. de Saint-Vincent, *Coherent control over the high-dimensional space of the nuclear spin of alkaline-earth atoms*, arXiv:2501.01731.

[67] C. Hofrichter, L. Rieger, F. Scazza, M. Höfer, D. R. Fernandes, I. Bloch, and S. Fölling, *Direct Probing of the Mott Crossover in the SU(N) Fermi-Hubbard Model*, *Phys. Rev. X* **6**, 021030 (2016).

[68] G. Pasqualetti, O. Bettermann, N. Darkwah Oppong, E. Ibarra-García-Padilla, S. Dasgupta, R. T. Scalettar, K. R. A. Hazzard, I. Bloch, and S. Fölling, *Equation of State and Thermometry of the 2D SU(N) Fermi-Hubbard Model*, *Phys. Rev. Lett.* **132**, 083401 (2024).

[69] J. Joykutty, V. Mathur, V. Venkataraman, and V. Natarajan, *Direct Measurement of the Oscillation Frequency in an Optical-Tweezers Trap by Parametric Excitation*, *Phys. Rev. Lett.* **95**, 193902 (2005).

[70] R. Grimm, M. Weidmüller, and Y. B. Ovchinnikov, *Optical dipole traps for neutral atoms*, in *Advances in atomic, molecular, and optical physics*, Vol. 42 (Elsevier, 2000) pp. 95–170.

[71] V. A. Dzuba and A. Derevianko, *Dynamic polarizabilities and related properties of clock states of the ytterbium atom*, *J. Phys. B* **43**, 074011 (2010).